Biophysical Journal, Volume *112*

Supplemental Information

Determining the Spatial Relationship of Membrane-Bound Aquaporin-4 Autoantibodies by STED Nanoscopy

John N. Soltys, Stephanie A. Meyer, Hannah Schumann, Emily A. Gibson, Diego Restrepo, and Jeffrey L. Bennett

SUPPORTING MATERIAL:

Determining the spatial relationship of membrane bound anti-aquaporin-4 autoantibodies by STED nanoscopy

John N Soltys[1], Stephanie A Meyer[2], Hannah Schumann[3], Emily A Gibson[2], Diego Restrepo[4], Jeffrey L Bennett[3,5]

[1]Medical Scientist Training and Neuroscience Graduate Training Programs, University of Colorado Anschutz Medical Campus, Aurora CO, USA

[2]Department of Bioengineering, University of Colorado Anschutz Medical Campus, Aurora CO, USA

[3]Department of Neurology, University of Colorado Anschutz Medical Campus, Aurora CO, USA

[4]Department of Cell and Developmental Biology, University of Colorado Anschutz Medical Campus, Aurora CO, USA

[5]Department of Ophthalmology, University of Colorado Anschutz Medical Campus, Aurora CO, USA

Materials and Methods

Antibodies: Recombinant monoclonal anti-AQP4 antibodies were produced from plasmablasts isolated from the cerebrospinal fluid of neuromyelitis optica patients [1]. Antigen and epitope specificities were identified as described [1, 2]. Four monoclonal recombinant antibodies (AQP4 rAbs #53, #58, #186, and #153) with unique epitope specificities [2] were selected for this study. For rAbs #53, #58, and #186, the E345R point mutation was introduced into the Fc region by site-directed mutagenesis (Life Technologies) and confirmed by DNA sequencing. The E345R mutation promotes the ordered assembly of antibodies on surface targets [3].

Crystal Schematics: Crystal structures of IgG1 (PDB ID: 1HZH) [4], AQP4 (PDB ID: 3GD8) [5], C1q globular head (PDB ID: 1PK6) [6], and collagen (PDB ID: 2D3H) [7] were used to generate schematics. C1q was assembled by approximating globular head/collagen assemblies based on known structures [6, 8]. For simplicity, the collagen stalk is removed from all C1q structures.

Sample Preparation and Immunohistochemistry:

Live Cell Staining: M1- and M23-AQP4 expressing CHO cells were cultured as described [2] and plated on #1.5 laminin-coated glass coverslips (neuVitro). The following day, media was washed twice, and AQP4 rAbs (2ug/mL and 10ug/mL) were bound to living cells for 30 minutes. Cells were then fixed in 4% PFA containing 0.1% gluteraldehyde for 15 minutes at 4C. Biotinylated Fab anti-human Fc domain (Novus Biologics) was used to detect bound AQP4 rAb and rabbit polyclonal antibody against the intracellular C-terminal domain of AQP4 (Santa Cruz) was used to label AQP4 tetramers and arrays. Primary antibodies were detected using streptavidin-conjugated Atto647N (Atto-tec) and goat anti-rabbit STAR 590 (Rockland Inc.).

Coverslips were mounted using ProLong Gold (LifeTech) supplemented with 2.5% DABCO, and rested 24 hours prior to imaging.

Fluorescent Beads and Atto647N: .02µm Fluospheres® carboxylate-modified microspheres filled with dark red fluorescent fluorophores (660/680; ThermoFisher F8783) were diluted and randomly immobilized onto poly-l-lysine coated #1.5 coverslips for 10 seconds. Mean bead diameter was reported as 28 +/- 4.6 nm by the manufacturer for the obtained Lot. Coverslips were mounted onto a glass slide +/- Atto647N fluorophore diluted serially in 1x PBS. 1x PBS in the absence of fluorophores was added to the mounting media for samples containing beads only.

Imaging with STED Nanoscope: Confocal and STED imaging was performed using the described home-built two-color STED nanoscope at the Anschutz Medical Campus Light Microscopy Core [9]. All images were generated with a pixel size of 19.52x19.52 nm unless otherwise specified. The color channels were initially designed for Atto 590 and Atto 647N fluorophores, and previously referred to as "Atto590 Channel" and "Atto647N Channel" although additional fluorophores may also be imaged in the designated channels. Here, we delineate the imaged fluorophores (Atto590, Atto647N, and dark red 660/680 that fills beads) instead of the instrument channel.

Analysis and Statistics: All image analyses and simulations were performed with MATLab_R2015a and MATLab_R2016b software (The MathWorks, Inc) using scripts coded in-house. Script integrity for rAb analyses was confirmed by comparing script data output for all image quantifications (as described below) with known distributions on artificially generated images containing multiple scenarios for pixel intensity organizations. Data was imported into Graphpad Prism 6 software to generate plots and perform statistical tests.

Fluorescent Bead +/- Atto647N Images:

Image Acquisition/Experimental Approach: At least 3 coverslips were made for each experimental condition and each coverslip was imaged in at least 2 locations (total of at least n=6 images analyzed for all experimental groups). The focal plane was determined by focusing on the 28 nm fluorescent beads. 3 coverslips were prepared without any fluorescent beads/fluorophores and were imaged at multiple planes to calculate background machine noise, after first sampling for the plane in which the most background signal could be detected. Confocal images were acquired first, followed by STED images. For repetitive imaging in the same field of view (3 images), STED imaging began immediately after sample focusing. Excitation power was 10µW and STED power 20mW.

Fluorescent Peak Analysis and Determination of Mean Peak FWHM: Images of 28nm beads alone were analyzed as described for 45nm polystyrene beads [9]. Briefly, all peaks within an image were identified, extracted as an 11 x 11 pixel ROI, and fit to a least squares 2D Gaussian using a MATLab program. However, the peak finding algorithm encountered problems in this study when analyzing objects smaller in size than those previously imaged [9]. Therefore, we returned to the standard approach of manual peak selection within the images [10-15] to quantify the appearance of Atto647N fluorophores imaged in the same focal plane as the larger 28nm beads. Identified peaks were fit to a least squares 2D Gaussian, the mean FWHM in the x and y

planes were quantified and averaged to calculate mean peak FWHM. Atto647N fluorophores were treated as point sources and mean peak FWHM calculations did not involve deconvolution.

AQP4 rAb Images:

Image Processing: The image processing approach was to first identify where AQP4 is expressed on the target cell using the intracellular AQP4 label (STAR590 channel), generate regions of interest (ROIs) by applying size inclusion (M23-AQP4) or size exclusion (M1-AQP4) filters to identify or eliminate OAPs respectively, and then analyze the spatial distributions of extracellular AQP4 autoantibodies (647N channel) within all ROIs. To maximize the number of detected autoantibodies (therefore minimizing analysis bias from low frequency spatial distributions of potential biologic significance), the 590 channel was not further processed beyond background noise subtraction with all remaining pixels containing an intensity value considered positive for an AQP4 tetramer. Stricter quantification did not change the data analysis (data not shown), likely attributable to the extensive processing criteria for scoring the Atto647N channel as described below.

AQP4 Tetramer and Array Analysis: On M1-AQP4, AQP4 tetramer clusters, at least 4 pixels in size, were identified and excluded from further analysis as these may represent leaky, low level M23-AQP4 expression and would potentially confound the analysis [16]. On M23-AQP4, OAPs that were at least 8 pixels in size were included to run all analyses. All included pixels were then used to mask the Atto647N channel to perform all analyses. At least n=3 cells per antibody were analyzed.

Quantification of rAb clustering via $FWHM^{rAb\ spread}$: A non-biased deconvolution algorithm was applied across the entire Atto647N image to eliminate user-bias, with the goal of quantifying gross object appearance across an entire image based on a maximum likelihood algorithm [17]. The output was a 2-dimensional array; the FWHM of a fit of this array to a 2D Gaussian distribution was calculated and termed $FWHM^{rAb\ spread}$, as distinct from the mean peak FWHM calculation discussed above. Although the predominant fluorescence signal drives the goodness of fit, it is possible that the calculation is driven by a smaller fraction of the fluorescence signal otherwise needed to recognize and quantify all image objects by eye. This could potentially produce a smaller than expected $FWHM^{rAb\ spread}$. Regardless, any observed shift in FWHM distribution represents a relative change in AQP4 rAb cluster size, because a larger $FWHM^{rAb\ spread}$ could only be generated from the same Atto647N fluorescence signal via summation of multiple fluorophores confined within a small surface area.

This analysis requires user input of the estimated mean object size, which was obtained by imaging Atto647N fluorophore alone and randomly immobilized antibodies as detailed above. However, this size is not necessarily reflective of the size of larger fluorophore densities that may label larger antibody clusters, therefore the analysis was repeated with multiple user estimations of object size. User object size approximations were the pixel dimensions for a 2-dimensional array, containing enough pixels in each dimension to fit a 2 dimensional Gaussian +/- 3 standard deviations from Gaussian peak.

For each experimental group, the calculated $FWHM^{rAb\ spread}$ met the following criteria: 1) the output array for all images had a general Gaussian appearance, i.e., a center peak bordered with

lesser values, 2) the calculated FWHM came from an array meeting the minimum size requirements to fit the respective Gaussian, and 3) the calculated $FWHM^{rAb\ spread}$ remained constant with increasing sizes of the user-input size estimate. The calculated $FWHM^{rAb\ spread}$ of each image was then averaged with the remaining images for each experimental group. For statistical comparisons, a one-way ANOVA was performed with Tukey's test for multiple comparisons (adjusted $p < .05$ considered significant, comparison alpha = .05).

Generation of Simulated Images to Determine of the Localization Efficiency of Fluorophores in Non-Resolvable Clusters: To analyze the spatial arrangements of bound autoantibodies in more detail, a scoring system was developed (as described below) whose application is dependent on the accurate localization of an individual fluorophore(s) to a single pixel. A data simulation was designed comparing known, random distributions of fluorophores (represented as a binary image) to the theoretical STED image obtained by that distribution. Fluorophores were modeled as being 12 nm in size, with random positioning requiring at least a 12 nm spacing between events. A cell was simulated with 100 distinct OAPs, and a random fluorophore distribution was generated over each OAP. To generate the theoretical STED image, each fluorophore was convolved to model the theoretical photon detection pattern based on the array appearance for autoantibody #58, and background noise was simulated. The representation of autoantibody #58 was selected because it closely resembles that of Atto647N alone, and the mean object size was consistent for both M1-AQP4 and M23-AQP4. STED pixel dimensions were then super-imposed, with each pixel representing the total sum of all photons in the pixel area.

Threshold Analysis of Simulated Images: After generating the simulated STED images, all pixels for the 647 channel (detecting simulated fluorophore distributions) contained a pixel intensity. We therefore asked if a threshold value could be applied that would accurately resolve fluorophore signal from background noise. Images were first deconvolved using the deconvolution algorithm array output for rAb #58 (see above), using a Lucy-Richardson deconvolution algorithm [18]. A series of simulations was performed in which the threshold intensity was increased at 5% increments starting at 5%, where any pixels with an intensity value below the threshold percent compared to the maximum pixel value on the OAP were reassigned a value of zero to exclude the point from the analysis. All remaining pixels were considered to contain a fluorophore. The resulting data set was compared to the binary STED image representing the true locations of all pixels containing fluorophores. For each image, the sensitivity (defined as the number of correctly identified fluorophore-containing pixels), false positive percentage (defined as the number of incorrectly identified fluorophore-containing pixels over the total number of identified pixels), and false negative rates (defined as the number of incorrectly missed fluorophore-containing pixels) were calculated.

Generation of the Antibody Spatial Arrangement (ASA) Score: A scoring system was developed to rank each pixel containing a fluorophore (as determined above) based on the potential for that pixel to participate in a multivalent interaction with the immune protein C1q. The ASA scale was devised based on approximate sizes of C1q-antibody complexes as previously reported from crystallization and cryo-EM studies [3, 19], compared with the size of each STED pixel. An ASA score of 1 represents an isolated pixel with no surrounding intensity signal, ASA Score 2: 2/4 pixels containing signal, ASA Score 3: 3/4 pixels containing signal, and ASA Score 4: 4/4 pixels containing signal. Each pixel received a final score based on the maximum possible ASA

score it could receive over a 2x2 pixel area, out of the 4 possible scores it could have been assigned.

The accuracy and sensitivity of this scoring system was tested by data simulation. A random distribution of fluorophores was generated and thresholded as described above (n=10 cells). ASA scores were then calculated for both the predicted localizations, and compared with the respective binary image. The initial ASA score demonstrated a systematic bias. A non-linear fit was applied to ASA scores 1 and 4, which were first normalized. Scores of 2 and 3 were normalized based on the final percent scored as a 1 or 4. The final scoring algorithm was tested on a second data simulation (n=10 cells), with results representing the goodness-of-fit for a linear regression of each ASA score.

ASA Scoring of Bound AQP4 Autoantibodies: All 647N images were deconvolved and thresholded as described above, using a 40% threshold. For M23-AQP4, each OAP across the entire image was scored individually with data output representing the mean percentage of ASA scores across all OAPs. M1-AQP4 does not form OAPs, therefore the ASA score was calculated across the entire cell. Data output represents the average ASA score distributions calculated for all images in the dataset. Cumulative ASA score distributions were compared using a Mann-Whitney test.

To identify how M23-AQP4 ASA image analysis may be impacted by threshold percentage value, deconvolved and raw were stepped through a series of thresholds and ASA score was calculated without score normalization.

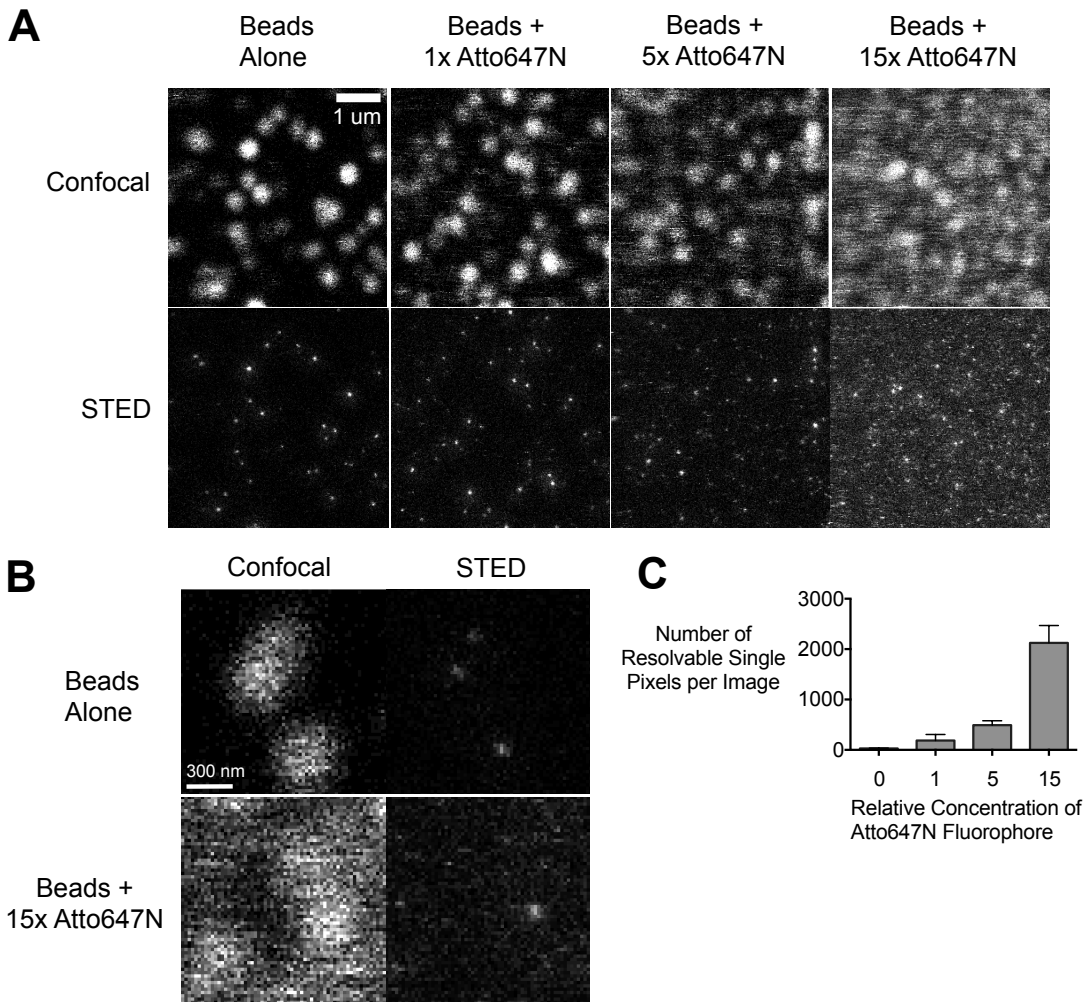

Supplemental Figure 1: Serial dilutions of Atto647N imaged in the same focal plane as 28nm beads

(A): Representative confocal (top) and STED (bottom) images of Atto647N fluorophores imaged in the same focal plane as 28nm beads. The concentration of beads was held constant across all coverslips while the concentration of Atto647N was serially diluted. The stated concentration represents the relative amount of Atto647N fluorophore on the respective coverslip. The scale bar in the top left image represents 1um and applies to all images. (B): Representative high magnification confocal and STED images for coverslips containing beads alone and for coverslips containing beads in addition to 15x Atto647N fluorophore. Scale bar in top left image represents 300nm and applies to all images. (C) The number of objects with fluorescent signal predominantly localizing over a single pixel was quantified for each image to ask if fluorophores may localize to single pixels, given that the majority of the signal attributable to fluorophores appeared to localize over single pixels as the concentration of Atto647N fluorophore increased. The number of resolvable single pixels increased in proportion to the concentration of fluorophores, supporting single pixel localization. Data is presented as the number of objects identified per individual image with n=6 images analyzed for each experimental group.

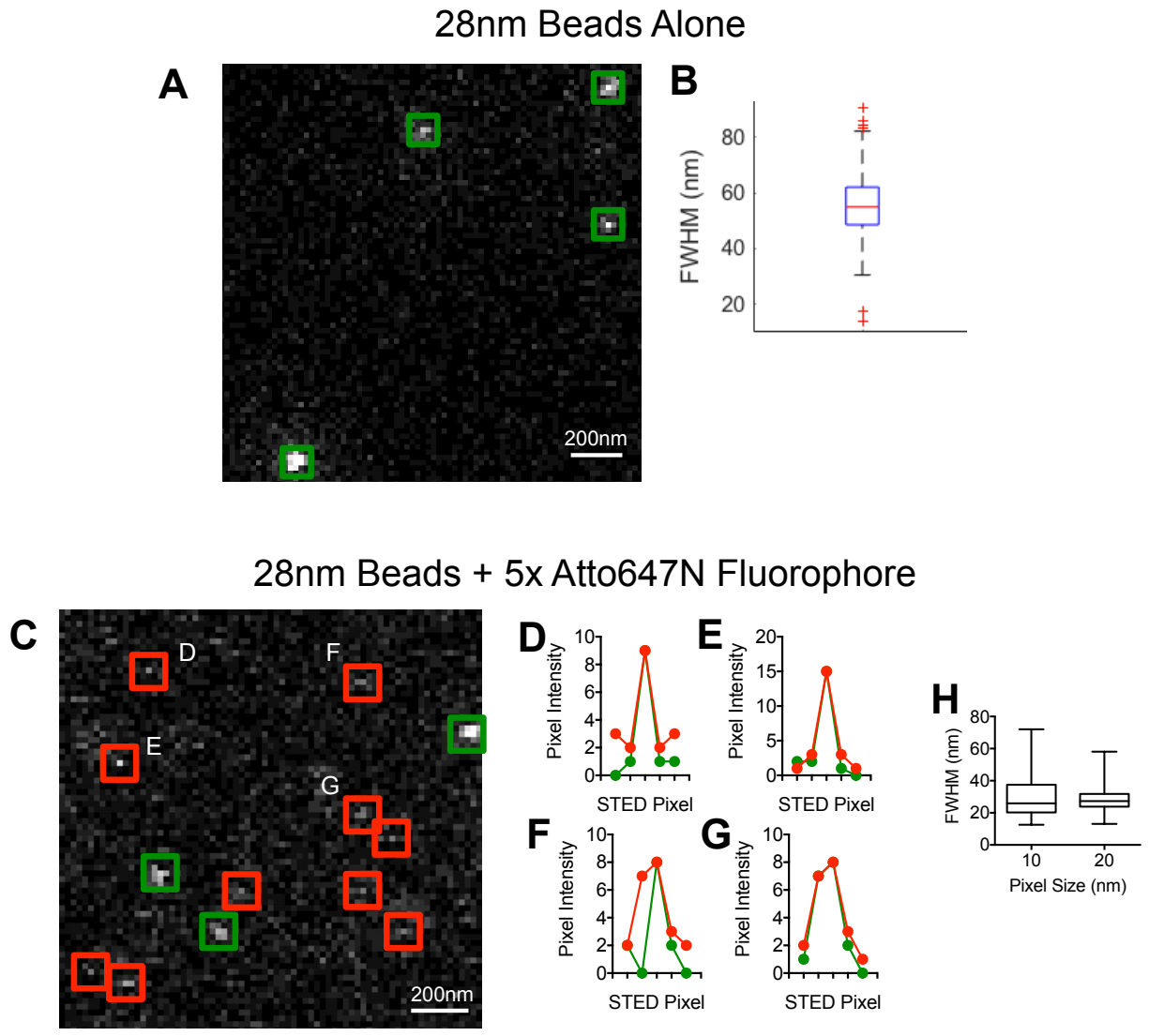

Supplemental Figure 2: Quantifying Atto647N fluorophore appearance
A representative image of a coverslip containing only beads filled with dark red 660/680 fluorophore is depicted in (A), scale bar = 200nm and pixel size = 20nm. Objects identified as beads are outlined in green. A mean peak FWHM of 55 +/- 11nm for a least squares 2D Gaussian fit was calculated for n=458 beads compiled across 6 images (B). However, the appearance of the distinct Atto647N fluorophore was of particular interest as the fluorophore labeled AQP4 rAb in the imaging model. A representative coverslip containing 5x Atto647N fluorophore in addition to 28nm beads filled with the distinct dark red 660/680 fluorophore is depicted in (C), scale bar = 200nm and pixel size = 20nm. All Atto647N fluorophore peaks must have a pixel intensity brighter than the brightest pixel identified when imaging blank coverslips to be considered for analysis, potentially biasing the calculation towards the brightest peaks. All qualified objects are outlined in red, larger objects identified by eye more consistent with the appearance of the larger beads are outlined in green. Importantly, both images (A) and (C) are sampled with identical criteria and no pixels in (A) appeared as isolated pixels that met sampling criteria to merit a red outline. All objects in the top half of image (C) are labeled D-G; pixel

intensity across the x and y direction is respectively plotted in (D-G). The box and whiskers plots depicted in (H) show the calculated mean peak FWHM for a least squares 2D Gaussian fit when sampling at 10 and 20 nm pixel sizes; calculated means are 28.2 +/- 7.3 (n=146) and 28.7 +/- 11.0 nm (n=156) respectively.

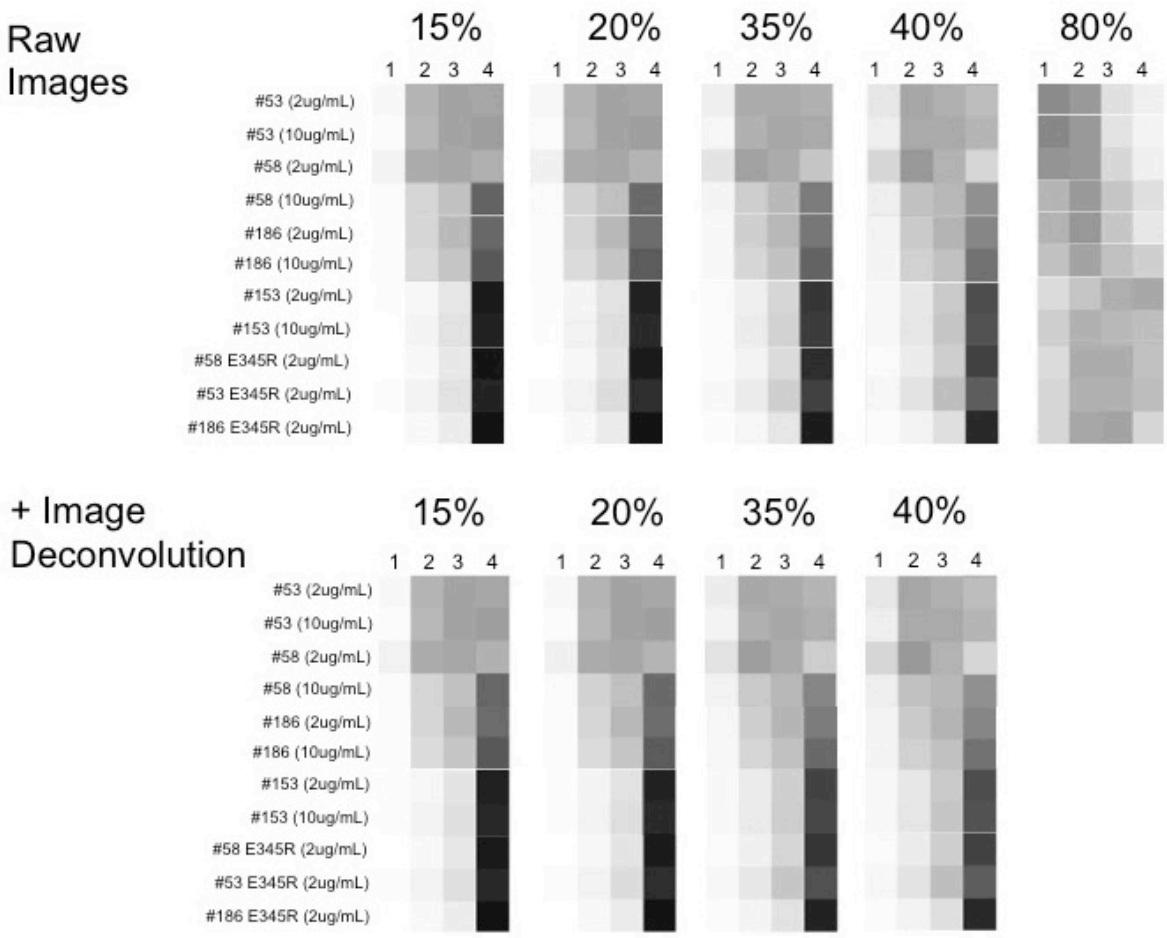

Supplemental Figure 3: ASA algorithm performance at a range of threshold intensities. Initial ASA score distributions were calculated at a range of threshold intensities on raw images (top) and on deconvolved images (bottom). The threshold percentage is indicated over the respective ASA score set.

SUPPORTING REFERENCES

1. Bennett, J.L., et al., *Intrathecal pathogenic anti-aquaporin-4 antibodies in early neuromyelitis optica*, in *Ann. Neurol.* 2009. p. 617-629.
2. Owens, G.P., et al., *Mutagenesis of the aquaporin 4 extracellular domains defines restricted binding patterns of pathogenic neuromyelitis optica IgG.*, in *J. Biol. Chem.* 2015. p. 12123-12134.
3. Diebolder, C.A., et al., *Complement is activated by IgG hexamers assembled at the cell surface.*, in *Science*. 2014. p. 1260-1263.
4. Saphire, E.O., et al., *Crystal structure of a neutralizing human IGG against HIV-1: a template for vaccine design.*, in *Science*. 2001. p. 1155-1159.
5. Ho, J.D., et al., *Crystal structure of human aquaporin 4 at 1.8 Å and its mechanism of conductance*, in *Proceedings of the ….* 2009.
6. Gaboriaud, C., et al., *The Crystal Structure of the Globular Head of Complement Protein C1q Provides a Basis for Its Versatile Recognition Properties*, in *Journal of Biological Chemistry*. 2003. p. 46974-46982.
7. Okuyama, K., et al., *High-resolution structures of collagen-like peptides [(Pro-Pro-Gly) 4-Xaa-Yaa-Gly-(Pro-Pro-Gly) 4]: Implications for triple-helix hydration and Hyp(X) puckering*, in *Biopolymers*. 2009. p. 361-372.
8. Rainey, J.K. and M.C. Goh, *A statistically derived parameterization for the collagen triple-helix*, in *Protein Science*. 2002.
9. Meyer, S.A., et al., *Super-resolution imaging of ciliary microdomains in isolated olfactory sensory neurons using a custom two-color stimulated emission depletion microscope.* Journal of Biomedical Optics, 2016. **21**(6): p. 066017-066017.
10. Wildanger, D., et al., *A compact STED microscope providing 3D nanoscale resolution.*, in *J Microsc*. 2009. p. 35-43.
11. Donnert, G., J. Keller, and R. Medda, *Macromolecular-scale resolution in biological fluorescence microscopy*, in *Proceedings of the ….* 2006.
12. Westphal, V., et al., *Dynamic far-field fluorescence nanoscopy*, in *New J. Phys.* 2007, IOP Publishing. p. 435.
13. Galiani, S., et al., *Strategies to maximize the performance of a STED microscope.*, in *Opt Express*. 2012. p. 7362-7374.
14. Willig, K.I., et al., *STED microscopy reveals that synaptotagmin remains clustered after synaptic vesicle exocytosis.*, in *Nature*. 2006. p. 935-939.
15. Harke, B., et al., *Resolution scaling in STED microscopy*, in *Optics ….* 2008.
16. Furman, C.S., et al., *Aquaporin-4 square array assembly: opposing actions of M1 and M23 isoforms.*, in *Proc. Natl. Acad. Sci. U.S.A.* 2003. p. 13609-13614.
17. Fahmy, M.F., et al., *A New Fast Iterative Blind Deconvolution Algorithm*, in *Journal of Signal and Information Processing*. 2012, Scientific Research Publishing. p. 98.
18. Fish DA, B.A., Pike ER, Walker JG, *Blind Deconvolution by Means of the Richardson-Lucy Algorithm.* Journal of the Optical Society of America a-Optics Image Science and Vision, 1995(12).
19. Pinteric, L., R.H. Painter, and G.E. Connell, *Ultrastructure of the Fc fragment of human immunoglobulin G.*, in *Immunochemistry*. 1971. p. 1041-1045.